The Cryosphere Discuss., 9, 4701–4731, 2015
www.the-cryosphere-discuss.net/9/4701/2015/
doi:10.5194/tcd-9-4701-2015

The Cryosphere Discussions
Open Access

Virtual radar ice buoys – a method for measuring fine-scale dynamic properties of sea ice

J. Karvonen

Finnish Meteorological Institute (FMI), Helsinki, PB 503, 00101, Finland

Received: 27 May 2015 – Accepted: 20 August 2015 – Published: 8 September 2015

Correspondence to: J. Karvonen (juha.karvonen@fmi.fi)

Published by Copernicus Publications on behalf of the European Geosciences Union.

Abstract

Here we present an algorithm for continuous ice dynamics estimation based on coastal and ship radar data. The ice dynamics are estimated based on automatically selected ice targets in the images. These targets are here called virtual buoys (VB's) and are tracked based on an optical flow method. To maintain continuous ice drift tracking new VB's are added after a given number of VB's have been lost i.e. they can not be tracked reliably any more. Some tracking results and some computed derived quantities for a few test cases are presented.

1 Introduction

Sea ice motion is an important parameter, because ice dynamics has a major effect on the nature of sea ice. Ice motion can cause ice pressure which in turn contributes to ice deformation, or diverging ice motion can cause opening of ice (cracks, leads). Here we represent a method to use coastal and ship radars for continuous monitoring of sea ice drift.

Marine radars typically operate at 10 GHz (wavelength $\lambda \approx 3$ cm) and 3 GHz ($\lambda \approx 10$ cm), i.e. at X and S bands. The radar resolution is defined by means of two resolutions, bearing and range resolutions. Bearing (a.k.a. as azimuth or angular) resolution is the ability of a radar system to separate objects at the same range, but at slightly different bearings. The bearing resolution depends on radar beam width and the range of the targets. Range resolution is the ability of a radar system to distinguish between two or more targets on the same bearing but at different ranges. Range resolution depends on the radar pulse length, unless radar pulse compression techniques (Cohen, 1987) are used. For digitizing the radar signal we have used a radar video server with a 20 MHz sampling rate. The radar server is Based on standard PC technology, and forms PPI (Plan Position Indicator) images from the radar signal, the radar triggering pulse and the radar antenna pulse. PPI is the most common type of radar display: the

TCD
9, 4701–4731, 2015

radar antenna is represented in the center of the display, so the distance from it can be presented as concentric circles.

If necessary, radar platform (ship) motion can be compensated based on the geoinformation (GPS position of each radar frame). However, large ship motion is not desirable because the radar signal is rapidly attenuated as a function of the range, or in the worst case the two radar images with a given time gap between them are not overlapping any more.

Relatively many publications on ice drift from Synthetic Aperture Radar (SAR) imagery and other satellite-borne EO data have been published. The motion estimation is based on detecting the same features in two adjacent images (e.g. Fily and Rothrock, 1987; Sun, 1994; Thomas et al., 2004, 2008; Karvonen, 2012). Motion vector estimation for weather radar data has also been studied, e.g. in Peura and Hohti (2004). Sea ice drift and object tracking from coastal radars has been studied earlier e.g. in Okhotsk Sea by matching of prominent features preserved from image to another (Tabata et al., 1980), in Barrow Sea using Lucas-Kanade optical flow algorithm (Lucas and Kanade, 1981) for features detected by Harris corner/edge detection (Harris and Stephens, 1988) algorithm (Rohith et al., 2013), and in Baltic Sea using a combination of phase-correlation and normalized cross-correlation (Karvonen, 2013a). One practical restriction for all the methods is that they can only operate where distinguishable objects exist, and in the featureless areas either no estimates are given, or the estimates are inter/extrapolated values. The motion detection methods are computationally intensive, but in principle easy to parallelize due to local nature of the computations.

In our earlier studies (Karvonen, 2013a; Karvonen et al., 2013) we have used data with longer temporal differences (10–30 min) than here, and an algorithm based on cross-correlation techniques. This approach was directly adapted from techniques used for ice drift estimation from SAR imagery (Thomas et al., 2004, 2008; Karvonen, 2012). However, with a finer temporal resolution sub-pixel resolution would be desirable, and it can not be achieved using cross-correlation techniques without suitable interpolation of the results. This interpolation needs to be nonlinear, thus also requiring

TCD
9, 4701–4731, 2015

a larger support area than a simple linear interpolation. Optical flow algorithm in turn inherently gives the estimates with a sub-pixel resolution. For this reason we found optical flow approach better suitable for fine temporal resolution radar imagery sea ice dynamics analysis.

2 Data sets used in the study

We have used three data sets to test the new algorithm. Two of the data sets were coastal radar data from the Tankar coastal radar, located at (63.95° N, 22.84° E): the first data set period was 25 February 2011 from 03:00 to 16:58 UTC (total time period of about 14 h), and the second data set period from 8 February 2012 from 00:00 to 23:58 UTC (total time period about one day). The data sets were selected such that they include significant ice drift. The temporal resolution of the two coastal radar data sets was 2 min. The third data set was a longer period data set and collected on-board RV *Lance* during the period from 21 January 2015, 11:30 UTC to 18 February 2015, 10:20 UTC. The temporal resolution of the RV *Lance* data set was 10 min. For demonstration purposes we selected a one-day period (8 February 2015 from 00:00 to 24:00 UTC) of the RV *Lance* data set. In this period set there also occurred significant and heterogeneous ice motion with respect to the ship within the radar coverage. During this one-day period the location of RV *Lance* was north of Svalbard, approximately 82.5° N, 18° E. The total range of the Tankar coastal radar data sets was 40 km and the image size was 1200 × 1200 pixels, i.e. the nominal resolution was 33.3 m. For the RV *Lance* radar the image size in pixels was the same as for the Tankar data, but the range was only 7.5 km, resulting to a nominal resolution of 12.5 m.

To reduce radar artifacts temporal median in the beginning of each minute (11 images, corresponding to about same amount of time in seconds, assuming that the radar rotation frequency is about 1 Hz) was performed. During this time period the ice motion is neglectable and only the noise and possible artifacts are reduced by the filtering. The images were also processed by homomorphic filtering to reduce the signal attenu-

TCD
9, 4701–4731, 2015

ation as a function of the range (Lensu et al., 2014). This processing mainly makes the visual analysis of the data easier. According to some performed tests it does not have significant effect on the tracking of objects.

For the RV *Lance* data we were unable to perform the temporal median filtering because we only had data with 10 min temporal sampling at our disposal, i.e. only one unfiltered image every ten minutes.

3 Weather and ice conditions on the test sites

The air temperature on 25 February 2011 around the Tankar lighthouse and radar station was from about −15 °C in the morning to about −3 °C in the afternoon. The previous day was colder with a daily maximum temperature of about −15 °C. The wind direction was 150–180°, and wind speed varied in the range 6–8 $m\,s^{-1}$. In the eastern parts of the area there was land fast ice, west of the fast ice there was a zone of very open ice (concentration 10–30 %), and west of this zone there were very close drift ice (concentration 90–100 %). The ice thickness in the area was 20–55 cm. The ice information were extracted from the FMI ice charts.

On 8 February 2012 the air temperature around the Tankar lighthouse and radar station was from −11° in the morning to −20 °C in the evening, also the previous day the temperatures were relatively cold, below −10 °C. The wind direction was 90–120°, and wind speed in the range 2–6 $m\,s^{-1}$. According to the FMI ice charts there was a fast ice zone in the eastern parts of the area, a zone of new ice to north and east of the fast ice, and very close drift ice further in the west. The ice thickness in the area was 5–30 cm.

On 8 February 2015 the air temperatures around RV *Lance* were cold, about −30 °C, the wind direction was 300–330° and wind speed around 8 $m\,s^{-1}$. The ship was drifting with a speed of approximately 0.2 $m\,s^{-1}$, first to the south and later to southeast. According to the met.norway ice charts the ice in the area was very close drift ice, and according to the operational Nansen Environmental and Remote Sensing Center

TCD
9, 4701–4731, 2015

(NERSC) Topaz ice model (Sakov et al., 2012) the ice thickness was 100–120 cm in the area.

4 Virtual buoys and tracking algorithm

We used an edge and corner detection to locate the VB's in the first radar image of a radar image sequence, and also when adding new VB's after the number of VB's has reduced to a predefined level (an adjustable parameter). The tracking algorithm is also based on the optical flow, e.g. Horn and Schunck (1981); Beauchemin and Barron (1985), between successive image pairs.

The flow diagram of our algorithm has been presented in the diagram of Fig. 1. In the first phase the VB's are initialized based on absolute local binary patterns (ALBP's) and then one iteration of motion tracking between the first two images of the image sequence is performed to prune the VB's due to noise amplification by the image filtering: all the images fed into the algorithm are first filtered by the homomorphic filtering to reduce the range dependence of the radar signal. After this initialization a list of the automatically selected VB's (including the locations and cross-correlations between the matched windows) are fed to the continuous VB tracking algorithm. At each iteration a new filtered radar image is put into the tracking system and the optical flow tracking between the previous and the novel image is performed. After each tracking iteration the number of resulting VB's is compared to a predefined threshold (T_N), and if the number of the remaining VB's is less than T_N, new VB's are added starting from near range until the original number of VB's has been reached. The new VB location are defined based on ALBP with the limitation that they are not allowed to be added closer than a given radius R_x (we have applied $R_x = 15$ pixels here, but this parameter can be defined by the user) from the existing VB's. After the VB adding step the tracking is continued with the updated list of VB's. If there still exist more VB's than then defined threshold, then the VB tracking is continued without updating the list of VB's.

TCD
9, 4701–4731, 2015

4.1 Local binary patterns and VB selection

We used local binary patterns (Ojala et al., 1996) in the edge and corner detection. We used a step of $\Pi/4$ corresponding to eight bit binary patterns, the radius R_{LBP} (distance from the center pixel, see Fig. 2) used here was two. A (8 bit) local binary pattern is defined as

$$\mathrm{LBP} = \sum_{k=0}^{7} s_1(g_k - g_c)2^k, \tag{1}$$

where g_c is the gray tone of the center pixel and the values of g_k are the gray tones in the eight pixels within the given radius R_{LBP} around the center pixel, see Fig. 2, and $s_1(x)$ defined as

$$s_1(x) = \begin{cases} 1, & \text{if } x \geq 0 \\ 0, & \text{if } x < 0. \end{cases} \tag{2}$$

Here we have used a variant which we here call the Absolute LBP (ALBP):

$$\mathrm{ALBP} = \sum_{k=0}^{7} s_2(g_k - g_c)2^k, \tag{3}$$

and $s_2(x)$ defined as

$$s_2(x) = \begin{cases} 1, & \text{if } |x| \geq T \\ 0, & \text{if } |x| < T \end{cases} \tag{4}$$

Rotational invariance can be achieved by using the minimum among all the (8) cyclic shifts of the ALBP. This is denoted here by ALBP_r. The values 15 of ALBP_r corresponds

TCD
9, 4701–4731, 2015

to an edge point, value 31 corresponds to a corner point, and value 63 corresponds to a sharp corner point.

As we wish the VB's to be traceable objects which do not to get mixed with other nearby features, we wish them to have a locally unique nonlinear structure with much corners. We select the points which locally (within a given radius R_b) maximize the complexity function F_c:

$$F_c(r,c) = N_c(r,c,R_s)N_{sc}(r,c,R_s), \quad (5)$$

where $N_c(r,c,R_s)$ is the number of corner points within a search radius R_s from the location described by the column and row coordinates (r,c), and $N_{sc}(r,c,R_s)$ is the number of sharp corner points within the same area. To avoid assigning VB's too close to each other, we only perform the search R_s or more outside the already assigned VB locations. We have used values $R_b = 30$ and $R_s = 15$ pixels here, but these parameters can be defined by the user.

VB's are added always when the number of VB's becomes less than a given threshold T_N. T_N can be defined as an absolute value or relative to the number of original VB's. In the experiments presented here we have used relative T_N values of 75–90 % of the number of the original number of the VB's.

Because we apply the homomorphic filtering prior to the VB selection, we also get relatively many VB's in the far range, because the filtering also amplifies the noise in the far range. For this reason we perform one tracking iteration between the first and second images of the sequence to remove the VB's due to this noise amplification. This first iteration removes the VB's generated by random fluctuation (amplified radar noise).

4.2 Optical flow and algorithm implementation

Optical flow (Horn and Schunck, 1981; Beauchemin and Barron, 1985) is a method used for estimating motion in image sequences such as in digital video. In optical flow

TCD
9, 4701–4731, 2015

we assume an intensity at a location (x, y) in a digital image at time to be moving such that

$$I(x, y, t) = I(x + \Delta x, y + \Delta y, t + \Delta t) \tag{6}$$

Using the Taylor expansion, and assuming small motion

$$I(x + \Delta x, y + \Delta y, t + \Delta t) = I(x, y, t) + \frac{\delta I}{\delta x}\Delta x + \frac{\delta I}{\delta y}\Delta y + \frac{\delta I}{\delta t}\Delta t + \text{HOT}$$
$$\Rightarrow \frac{\delta I}{\delta x}\Delta x + \frac{\delta I}{\delta y}\Delta y + \frac{\delta I}{\delta t}\Delta t = 0, \tag{7}$$

HOT stands for higher than first order terms. Dividing by Δt we get the optical flow equation:

$$I_x v_x + I_y v_y = -I_t, \tag{8}$$

where I_x, I_y I_t indicate the partial derivatives of the image signal with respect to x, y, and t. The changes of I at (x, y) in x and y directions and change of I in time can be estimated from an image pair. To perform the estimation additional conditions are needed. One practical approach is the Lucas-Kanade method (Lucas and Kanade, 1981) where it is assumed that optical flow equation holds for a block of N pixels p_k $(k = 1, \ldots, N)$:

$$\begin{aligned} &I_x(p_1)v_x + I_y(p_1)v_y = -I_t(p_1) \\ &\qquad \ldots \\ &I_x(p_N)v_x + I_y(p_N)v_y = -I_t(p_N) \end{aligned} \tag{9}$$

This corresponds to a (overdetermined) linear system Av=b. And can be solved (least squares solution) (Penrose, 1955) as

$$v = (A^T A)^{-1} A^T b = Mb, \tag{10}$$

TCD
9, 4701–4731, 2015

$M = (A^T A)^{-1} A^T$ is known as the Moore-Penrose pseudoinverse.

We have used the following discrete estimates for I_x, I_y and I_t (Horn and Schunck, 1981):

$$
\begin{aligned}
I_x =& (I_1(r+1,c) - I_1(r,c) + I_1(r+1,c+1) - I_1(r,c+1) + \\
& I_2(r+1,c) - I_2(r,c) + I_2(r+1,c+1) - I_2(r,c+1))/4 \\
I_y =& (I_1(r,c+1) - I_1(r,c) + I_1(r+1,c+1) - I_1(r+1,c) + \\
& I_2(r,c+1) - I_2(r,c) + I_2(r+1,c+1) - I_2(r+1,c))/4 \\
I_t =& (I_2(r,c) - I_1(r,c) + I_2(r+1,c) - I_1(r+1,c) + \\
& I_2(r,c+1) - I_1(r,c+1) + I_2(r+1,c+1) - I_1(r+1,c+1))/4
\end{aligned}
\tag{11}
$$

where I_1 and I_2 are the first and second (in this temporal order) image of an image pair, (r,c) refers to the row and column coordinates which are used here instead of x and y. The image pixel values with fractional coordinates are computed using bi-linear interpolation. For numerical stability it is essential that the estimates for I_x, I_y and I_t are computed at the same spatiotemporal location.

The optical flow method is best suitable for short motion corresponding to short time differences, e.g. for our coastal radar data with a relatively short short time difference (in our case 2 min). In practice some image smoothing at sharp edges is recommendable before the optical flow computation, because optical flow assumes continuity of the signal. For this reason we perform a spatial Gaussian smoothing of the images before the optical flow estimation. The Gaussian smoothing is combined with the original image data by a linear combination to get the smoothed pixel value $I'(r,c)$ from the original pixel value $I(r,c)$ and the smoothed pixel value $G(r,c)$:

$$
I'(r,c) = fG(r,c) + (1-f)I(r,c). \tag{12}
$$

We used a Gaussian kernel with standard deviation $\sigma = 15.0$ (pixels) in the Gaussian smoothing, and for the factor $f = 0.8$.

TCD
9, 4701–4731, 2015

In computation of the optical flow we used a spherical window with a radius of 11 pixels (resulting to $N = 377$) for the coastal radar data and a a spherical window with radius of 21 pixels ($N = 1373$) for the ship radar (with longer time difference between the successive images) in the optical flow estimation.

If the cross-correlation between two matched windows is less than a given threshold T_{cc} the object is not tracked any more, i.e. the VB is lost. We have used $T_{cc} = 0.9$ in our experiments presented here. We also studied the use of the coefficient of determination of the linear fits as a measure of the matching quality, but it seems to have insignificant correlation e.g. with respect to the cross-correlation, which seems to be a more useful measure. The first tracking iteration (between the first and second images) is used to prune the unreliable VB's produced by noise amplification due to the homomorphic filtering. The same cross-correlation thresholding is applied for this purpose.

5 Experimental results

5.1 Coastal radar image sequences

The initial radar images (first images in the image sequences) of the two coastal radar image sequences of 25 February 2011 and 8 February 2012, with the locations of the initial VB's indicated, used in our experiments are shown in Fig. 3. The location of the radar indicated by the green dot and the initial VB's are indicated by red dots and the location of the radar by green dots.

The first and last images of the 25 February 2011 and the 8 February 2012 cases are shown in Figs. 4 and 5, respectively. From these images we can see the change of the ice field during the whole study periods. In the 11 February 2011 case a large ice field is torn off and drifting away from the land and land fast ice zone. In the 8 February 2012 case a smaller part of the ice is also torn off and floating away from the coast. The trajectories resulting from the Lucas-Kanade optical flow algorithm for the two test cases are shown in Fig. 6a and b. We can see that for the 25 February 2011 case

TCD
9, 4701–4731, 2015

the direction of the motion was rather uniform over the whole drift ice area, but for the 8 February 2012 case the direction of the motion was less uniform. However, this kind of trajectory plots do not show the ice drift velocity evaluation as a function of time.

The VB trajectories computed by the algorithm correspond to the visual interpretation during the test periods. The visual inspection was performed using animations of the image sequences with the VB's indicated by colored circles over the radar imagery. The information derived from VB's gives us possibilities to estimate different parameters related to the ice dynamics. We have computed some features for three selected VB's on both the images. Three VB's were selected to initially be close each other such that they form a triangle. Based on the triangles formed by the VB triplets we could compute the evolution of the area of the triangles as a function of time, indicating local divergence or convergence. The trajectories of the selected VB triplets are indicated by red color in Fig. 6.

For the 25 February 2011 case a large part of the ice was torn off the fast ice and drifting to northwestern direction (Figs. 4 and 6a). For this case we applied a threshold $T_N = 75\,\%$ of the original number of VB's. The number of VB's as a function of the 2 min time steps for this case is shown in Fig. 7a. We adjusted T_N this high just to demonstrate the adding of VB's, in practice a lower value could be used. for the 8 February 2012 case some smaller ice floats were torn off and drifting to west and southwest (Figs. 5 and 6b). For this case we used $T_N = 90\,\%$ of the original number of VB's. The number of VB's as a function of 2 min time steps is shown in Fig. 7b. Because the total time was longer for this case the VB's were added twice during the whole time period of 24 h.

It is also straightforward to compute the velocity and direction (here given as the compass direction with zero degrees to the north, 90° to east and so on) by just dividing the displacement converted to meters by the time step of two minutes for each successive image pair. The velocities and direction for the selected three VB's of 25 February 2011 case are shown in Fig. 8. It can be seen that the three VB's are moving rather coherently. The velocity is first very slow and the direction rather ambiguous. Then the velocity is accelerated rather rapidly (the acceleration could also be estimated by di-

TCD
9, 4701–4731, 2015

viding the velocity differences between the two adjacent velocities by the time step, if necessary). It can also be seen that as the direction changes for a short time, the velocity is reduced (around time step 300). In Fig. 9 the velocity and direction are shown for the 8 February 2012 case. Also in this case the ice is quite stable for a while in the beginning of the time period and then the velocity accelerates to a top value of about 0.3 $m\,s^{-1}$ achieved near the end of the period. For the 25 February 2011 case the top velocity was a little lower and achieved about in the middle of the time period. For the 8 February 2012 case the velocities of the three studied VB's were less uniform than for the 25 February 2011 case. This also results to the larger divergence for this case compared to 25 February 2011 case. The area of the triangle formed by the three studied VB's in this case increases up to about 1.5 times the original triangle size, for the 25 February 2011 case the area only increases to about 1.2 times the original size. These numbers indicate slight divergence in both the cases.

5.2 Ship radar image sequence

The RV *Lance* ship radar data was collected during the period from 21 January to 18 February, and the temporal difference between each image pair was 10 min which is quite long for an optical flow algorithm. The ship was drifting in ice and no ship motion correction based on ship GPS has been performed, i.e. the detected ice drift is the drift with respect to the ship. We computed the tracking for the whole period but here we only show the results for a one day period with some interesting motion. During many of the days the motion with respect to the ship was not significant. Because the ship radar had a shorter range and higher resolution there were sea ice details visible over the whole image. For demonstration we selected the 8 February 2015 data for the whole day with significant ice motion with respect to the ship is some areas within the ship radar range. Also in this case we selected three adjacent VB's, indicated by red color in the trajectory image of Fig. 12, for which we computed their velocities, directions and the divergence based on the area of the triangle formed by these three VB's. The first image of the one day time period (8 February 2015, 00:00 UTC) and the last image of

TCD
9, 4701–4731, 2015

the period (9 February 2015, 00:00 UTC) are shown in Fig. 11. It can be seen that two larger leads are opening, one in the northeastern part and another in the southern part of the images. This is also indicated by the VB trajectories shown in Fig. 12. The drift velocity, direction and divergence for the selected VB triplet are shown in Figs. 13 and 14. In this case the direction changes quite suddenly around time step 60. However, there is no significant reduction in the computed drift velocity. This may be due to the relatively sparse time step of 10 min, with 2 min time steps the speed change might have been larger. It can also be seen that there occur some compression for the ice area described by the selected triplet of VB's. The area is decreased to about 80 % of the original area. This is because the VB's belong to the ice field east of the opening lead and the ice is compressing in this area.

6 Discussion and conclusions

A novel algorithm for ice tracking was developed to track virtual ice buoys. The algorithm enables continuous ice dynamics tracking by adding VB's after certain absolute or relative amount of VB's has been lost, this number or ratio can be defined by the algorithm user. The location of the VB's are initialized automatically based on the local information content of the image favoring location with well-distinguishable features. The VB's can also be initialized manually if some specific case studies are made. This method is best suitable for relatively short temporal steps and giving sub-pixel resolution, unlike our earlier algorithm based on cross-correlation (Karvonen, 2013a). From the VB tracks many kinds of derived quantities can be computed, and information on the nature of the ice dynamics extracted. For example it is possible to distinguish between deformed ice and level ice or open water at least in the near range area, and also opening of new open water channels can be identified.

We applied the developed algorithm to three test cases. Here we only computed some relatively simple derived quantities related to the ice dynamics, i.e. velocity, direction, and the relative area defined by triplets of VB's. The relative area gives infor-

TCD
9, 4701–4731, 2015

mation on the divergence and convergence of the ice, and also at some degree on the compression in the ice. Some other and more sophisticated ways to analyze VB data have been presented e.g. in Karvonen et al. (2013). The main purpose of this study was the development of the VB tracking system.

The VB drift results for the test cases were evaluated based on visual inspection of the animations of the image sequences with overlaid VB positions. There were no real buoy data available. The visual analysis showed that the algorithm results correspond to the visual interpretation and same targets were tracked throughout the radar image sequences. This could also be visually verified by extracting single frames of the radar image time series with a time difference of e.g. 2–3 h, and with some given VB positions indicated on the radar images. Also according to this verification the algorithm tracking results and visual inspection were in good agreement.

This VB tracking software complemented with some basic VB data analysis software tools will be included in the radar servers making automated ice dynamics analysis in real-time or near-real-time possible. The analysis tools will include the analysis of VB drift velocity and direction, and divergence based on triangles formed by VB triplets. These will be computed within the convex polygon defined by the outer VB's in the image in a given grid and for a given time step (multiple of the basic time step). This integration is under construction as part of the project "Harnessing Coastal Radars for Environmental Monitoring Purposes" (HARDCORE) funded by the Baltic Sea Research and Development Programme (BONUS).

References

Beauchemin, S. S. and Barron, J. L.: The Computation of Optical Flow, ACM New York, USA, 1985. 4706, 4708

Cohen, M. N.: Principles of Modern Radar Systems, Chapman and Hall, New York, USA, 465–501, 1987. 4702

Fily, M. and Rothrock, D. A.: Sea ice tracking by nested correlations, IEEE T. Geosci. Remote, 5, GE-25, 570–580, 1987. 4703

TCD
9, 4701–4731, 2015

Haarpaintner, J.: Arctic-wide operational sea ice drift from enhanced-resolution QuikScat/SeaWinds scatterometry and its validation, IEEE T. Geosci. Remote, 44, 102–107, 2006.
Harris, C. and Stephens, M.: A combined corner and edge detector, Proc. of Alvey Vision Conference, Univ. of Manchester, 31 August–2 September 1988, Manchester, UK, 147–151, 1988. 4703
Horn, B. K. P. and Schunck, B. G.: Determining optical flow, Artif. Intell., 17, 185–203, 1981. 4706, 4708, 4710
Karvonen, J.: Operational SAR-based sea ice drift monitoring over the Baltic Sea, Ocean Sci., 8, 473–483, doi:10.5194/os-8-473-2012, 2012. 4703
Karvonen, J.: Tracking the motion of recognizable sea-ice objects from coastal radar image sequences, Ann. Glaciol., 54, 4149 pp., 2013. 4703, 4714
Karvonen, J., Heiler, I., Haapala, J., and Lehtiranta, J.: Ice objects tracked from coastal radar image sequences as virtual ice buoys, Proc. of The International Conferences on Port and Ocean Engineering under Arctic Conditions (POAC'13), abstract number POAC13_030, 9–13 June 2013, Espoo, Finland, 2013. 4703, 4715
Lensu, M., Heiler, I., and Karvonen, J.: Range compensation in pack ice imagery retrieved by coastal radars, in: Proc. IEEE Baltic International Symposium (BALTIC), 27–29 May 2014, Tallinn, Estonia, 1–5, 2014. 4705
Lucas, B. and Kanade, T.: An iterative image registration technique with an application to stereo vision, in: Proceedings of the 7th International Joint Conference on Artificial Intelligence (IJCAI) 1981, 24–28 August, Vancouver, Canada, vol. 2, 674–679, 1981. 4703, 4709
Ojala, T., Pietikainen, M., and Harwood, D.: A comparative study of texture measures with classification based on feature distributions, Pattern Recogn., 29, 51–59, 1996. 4707
Penrose, R.: A generalized inverse for matrices, P. Camb. Philos. Soc., 51, 406–413, doi:10.1017/S0305004100030401, 1955. 4709
Peura, M. and Hohti, H.: Optical flow in radar images, in: Proc. Third European Conference on Radar in Meteorology and Hydrology (ERAD2004), Copernicus, 454–458, 6–10 September 2004, Visby, Sweden, 2004. 4703
Rohith, M. V., Jones, J., Eicken, H., and Kambhamettu, C.: Extracting quantitative information on coastal ice dynamics and ice hazard events from marine radar digital imagery, IEEE T. Geosci. Remote, 51, 2556–2570, 2013. 4703

TCD
9, 4701–4731, 2015

Sakov, P., Counillon, F., Bertino, L., Lisæter, K. A., Oke, P. R., and Korablev, A.: TOPAZ4: an ocean-sea ice data assimilation system for the North Atlantic and Arctic, Ocean Sci., 8, 633–656, doi:10.5194/os-8-633-2012, 2012. 4706

Sun, Y.: A new correlation technique for ice-motion analysis, EARSeL Adv. Remote Sens., 3, 57–63, 1994. 4703

Tabata, T., Kawamura, T., and Aota, M.: Divergence and rotation of an ice field off Okhotsk Sea Coast of Hokkaido, annals of glaciology, in: Sea Ice Processes and Models, University of Washington Press, Seattle, USA, 273–282, edited by: Pritchard, R. S., 1980. 4703

Thomas, M., Geiger, C., and Kambhamettu, C.: Discontinuous non-rigid motion analysis of sea ice using C-band synthetic aperture radar satellite imagery, IEEE Workshop on Articulated and Nonrigid Motion (ANM, In conjunction with IEEE CVPR'04), 27 June–2 July 2004, Washington DC, USA, available at: http://vims.cis.udel.edu/publications/anm-thomas.pdf (last access: 7 September 2015) 2004. 4703

Thomas, M., Geiger, C. A., and Kambhamettu, C., High resolution (400 m) motion characterization of sea ice using ERS-1 SAR imagery, Cold Reg. Sci. Technol., 52, 207–223, 2008. 4703

TCD
9, 4701–4731, 2015

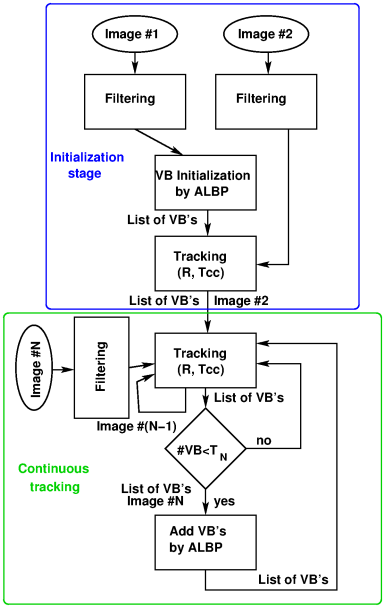

Figure 1. Flow diagram of the continuous VB tracking.

TCD
9, 4701–4731, 2015

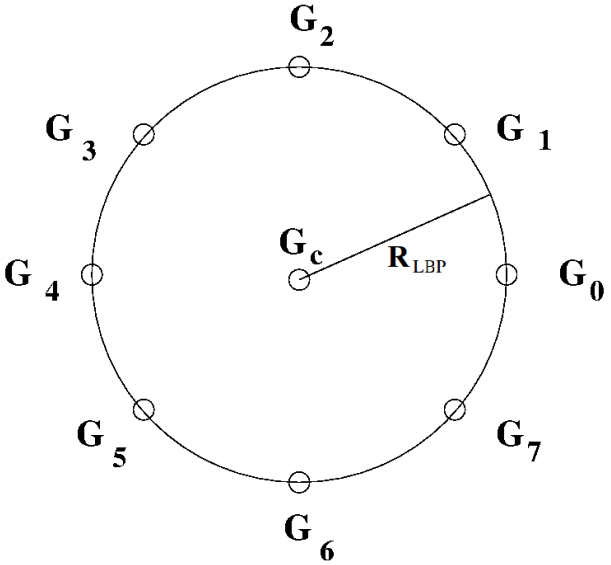

Figure 2. Geometry of an LBP with an angular step of Π/4. The circle has a radius of R, which is one LBP parameter.

TCD
9, 4701–4731, 2015

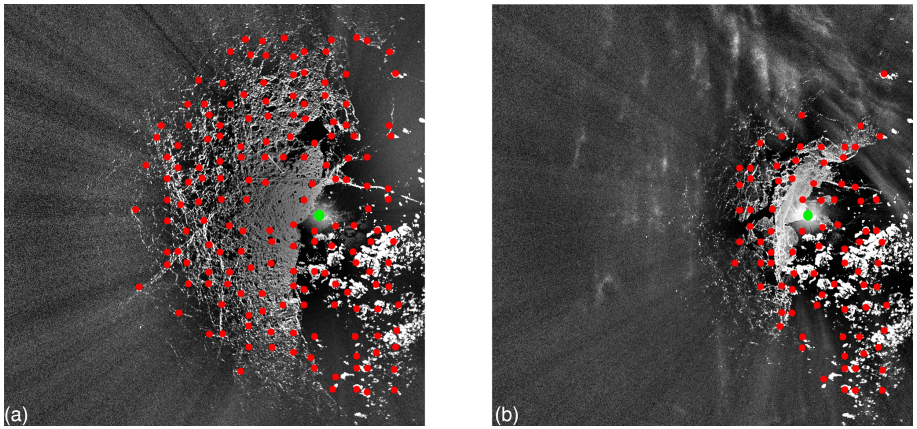

Figure 3. The initial VB's of the February 2011 test data set **(a)**, and the February 2012 data set **(b)** drawn over the first radar images of the sequences. The radar location is indicated by the green dot in the figures.

TCD
9, 4701–4731, 2015

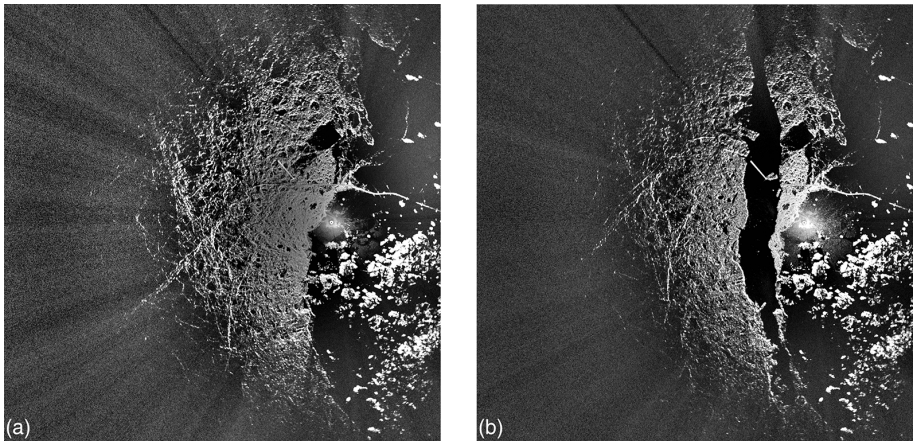

Figure 4. The first and last image of the February 2011 test data set.

TCD
9, 4701–4731, 2015

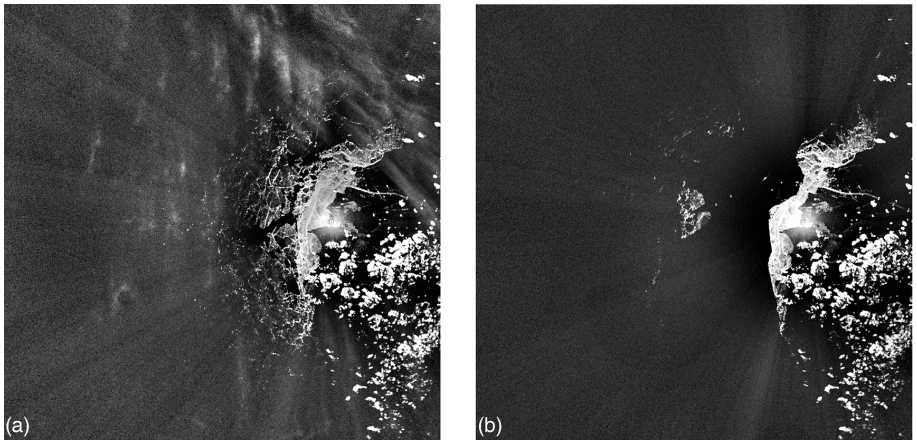

Figure 5. The first and last image of the February 2012 test data set.

TCD
9, 4701–4731, 2015

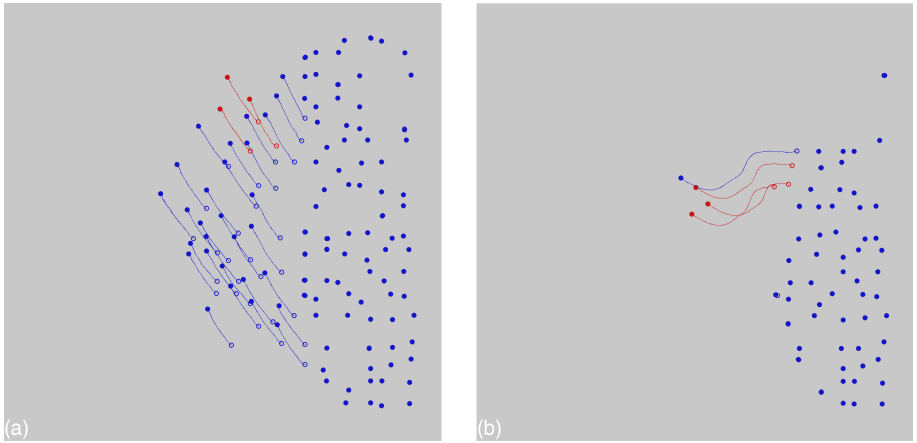

Figure 6. Trajectories of the VB's which survived the whole February 2011 and February 2012 test periods. The three VB's whose properties are studied in more detail in both the cases are indicated by red color. The starting point of a trajectory is indicated by an open circle and the end point by a closed circle.

TCD
9, 4701–4731, 2015

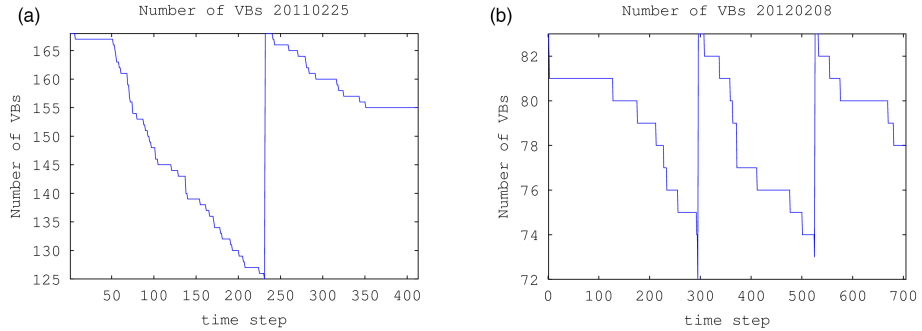

Figure 7. Number of VB's at each time step for the 2011 case **(a)** and for the 2012 case **(b)**. The threshold to add new VB's was 75 and 90 % of the original number of VB's, respectively.

TCD
9, 4701–4731, 2015

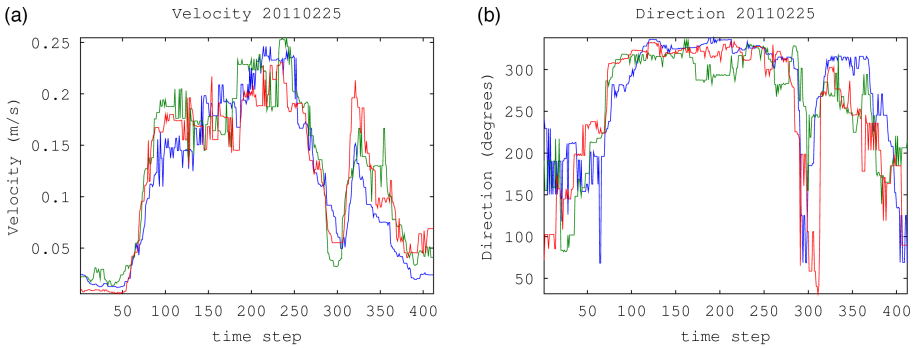

Figure 8. Velocity **(a)** and direction **(b)** for the 2011 case selected three VB's. The direction is in degrees.

TCD
9, 4701–4731, 2015

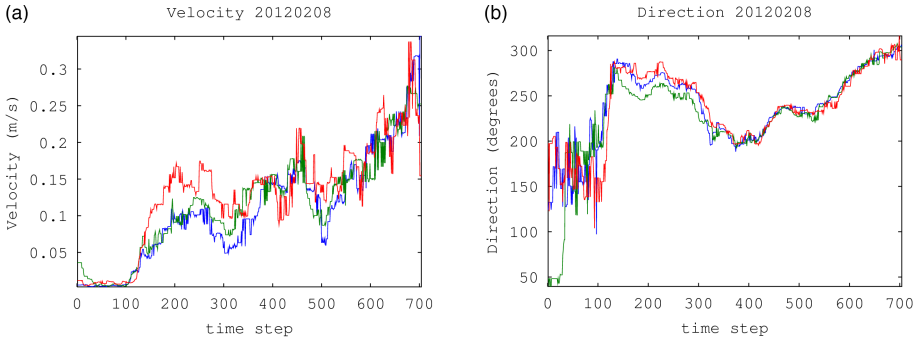

Figure 9. Velocity **(a)** and direction **(b)** for the 2012 case selected three VB's. The direction is in degrees.

TCD
9, 4701–4731, 2015

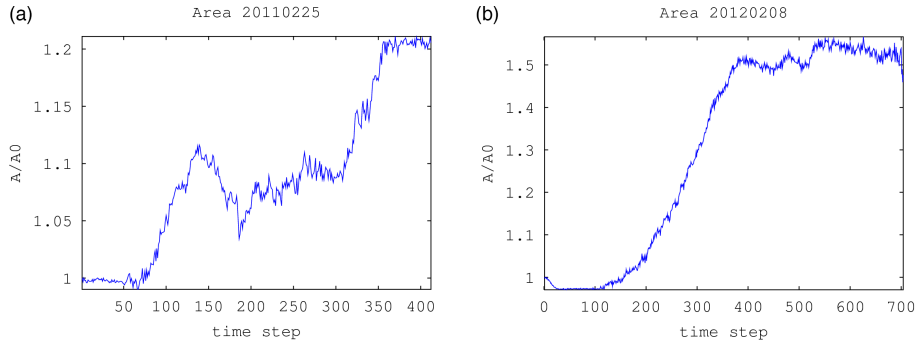

Figure 10. Ratio of the area of the triangle formed by the selected three VB's with respect to the area in the beginning of the period for the 2011 case **(a)** and for the 2012 case **(b)**.

TCD
9, 4701–4731, 2015

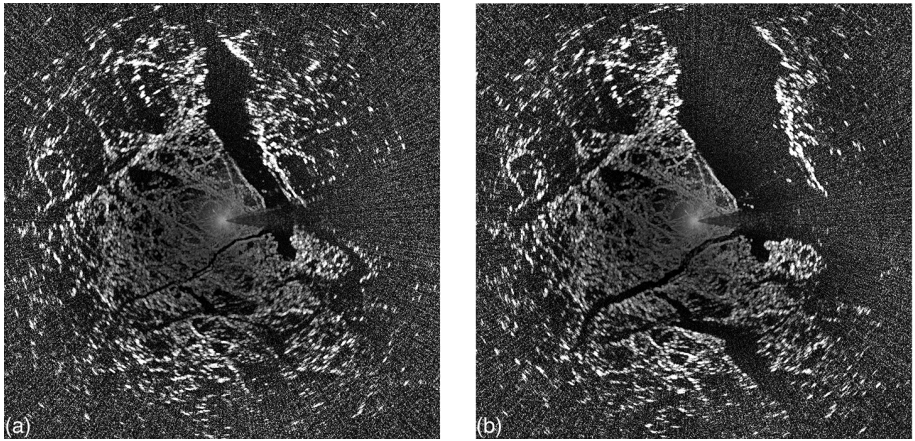

Figure 11. The RV *Lance* one day test period first and last radar images. The ship radar is located in the middle of the image.

TCD
9, 4701–4731, 2015

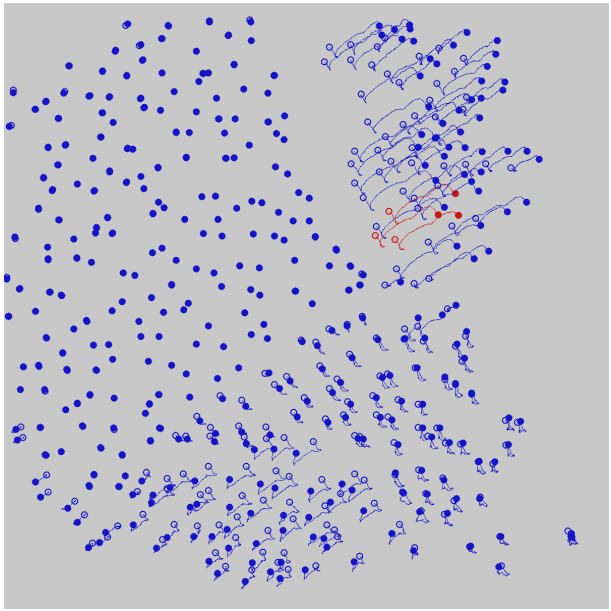

Figure 12. Trajectories of the VB's which survived the RV *Lance* one-day February 2015 test periods. The three VB's whose properties are studied in more detail in both the cases are indicated by red color. The starting point of a trajectory is indicated by an open circle and the end point by a closed circle.

TCD
9, 4701–4731, 2015

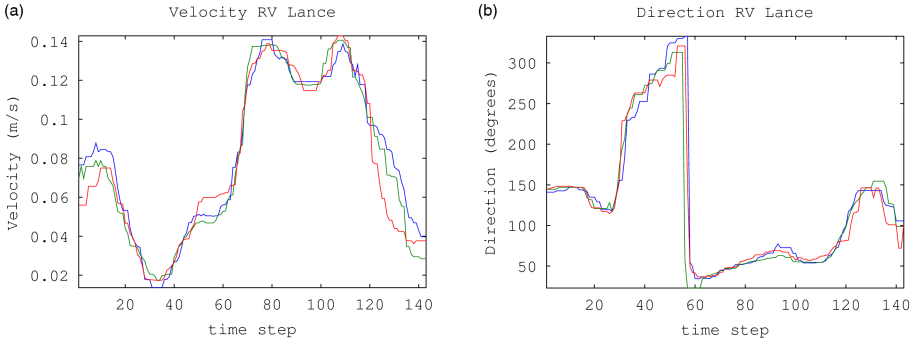

Figure 13. Velocity **(a)** and direction **(b)** for the RV *Lance* 2015 case selected three VB's. The direction is in degrees.

TCD
9, 4701–4731, 2015

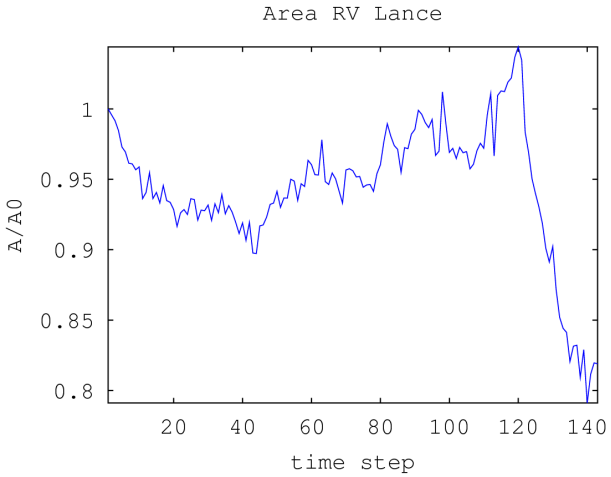

Figure 14. Ratio of the area of the triangle formed by the selected three VB's with respect to the area in the beginning of the period for the 2015 RV *Lance* case.

TCD
9, 4701–4731, 2015